

STUDY OF THE MPD DETECTOR CAPABILITIES FOR ELECTRON–POSITRON PAIR MEASUREMENTS AT THE NICA COLLIDER

*V. Vasendina*¹, *V. Jejer*, *V. Kolesnikov*,
S. Lobastov, *G. Musulmanbekov*, *I. Tyapkin*, *A. Zinchenko*

Joint Institute for Nuclear Research, Dubna

One of the main tasks of the NICA/MPD physics program is a study of low-mass vector mesons ρ , ω , ϕ by measuring their dileptonic decay channels. In this paper, the current status of simulations of electron–positron pair measurements in MPD is presented and the detector performance for such measurements is discussed.

Одной из основных задач в физической программе эксперимента MPD на комплексе NICA является изучение векторных мезонов с малой массой ρ , ω , ϕ с использованием их лептонной моды распада. В работе представлен статус моделирования измерений электрон–позитронных пар в MPD и обсуждаются возможности детектора для этих измерений.

PACS: 24.10.Lx; 25.75.Cj; 25.75.Dw; 29.85.Fj

INTRODUCTION

The main goal of the NICA (Nuclotron-based Ion Collider fAcility) heavy-ion program at JINR is an experimental investigation of the properties of nuclear matter under extreme conditions [1]. The existence of a new phase of matter, the Quark–Gluon Plasma (QGP), is predicted at sufficiently high temperature and/or baryon density, which could be realized in heavy-ion collisions. As the NA49 experiment has reported, the results on charged pion and kaon production in central Pb + Pb collisions may indicate onset of deconfinement at low SPS energies [2]. Such a phase transition might be accompanied by restoration of chiral symmetry due to melting of the quark condensate at the transition temperature [3]. The correlated e^+e^- or $\mu^+\mu^-$ pairs (*dileptons*), especially those from decays of vector mesons (ρ , ω , ϕ), are the best candidates to relate medium modifications of hadronic spectral function to the restoration of the chiral symmetry in $A + A$ collisions [4–6]. The ρ meson plays the central role in these studies because of its short lifetime ($c\tau = 1.3$ fm) and high probability to decay inside the reaction zone. The invariant-mass distribution of electron–positron pair reflects the mass distribution of the vector meson at the moment of the decay, and since the ρ decay products (i.e., electrons and positrons) interact only electromagnetically, they escape the interaction

¹E-mail: vasveron@mail.ru

region unaffected by subsequent strong interactions in dense hadronic matter and carry to the detectors information about the conditions and properties of the medium at the time of their creation. From the theoretical point of view, the question of how and to what extent the ρ -meson spectral function has changed in dense nuclear matter is under debate; however, no definite conclusion about the underlying mechanism could be drawn, e.g., broadening of the ρ spectral function due to hadronic interactions [5,6] or dropping of its mass [4].

Production of low-mass dileptons ($M_{e^+e^-} < 1.2 \text{ GeV}/c^2$) in heavy-ion collisions has been studied at the CERN-SPS at $\sqrt{s} = 8.8A, 17A$ and $19A$ GeV [7–11]. The CERES collaboration has observed a strong excess in the invariant-mass spectrum of electron-positron pairs in the region $0.2 < M_{e^+e^-} < 0.7 \text{ GeV}/c^2$ above the expectations from the superposition of the known hadron decay channels based on their vacuum properties. Moreover, a stronger enhancement observed at $8.8A$ GeV indicates sensitivity of the physics signal to the baryon density attained in the reaction. At the Brookhaven Lab., the PHENIX [12] and STAR [13] experiments measured the dilepton production from the top RHIC energy ($\sqrt{s} = 200A$ GeV) down to the top SPS energy, and also reported on the excess in e^+e^- spectra below the ω meson. The STAR measurements at $\sqrt{s} = 19A$ GeV are comparable to CERES and consistent with in-medium ρ -broadening by its scattering off baryons. The dilepton spectra from the DLS [14] and HADES [15] experiments taken at much lower incident energies ($1\text{--}2A$ GeV) in smaller colliding systems (C+C and Ar+Ar) are well described by a superposition of elementary nucleon-nucleon collisions, in contrast to higher energies and heavier nuclei. Until now, no dilepton measurements have been performed at AGS and low SPS energies, and the NICA-MPD dilepton program is aimed at closing this gap. The chosen range of collision energies ($4 < \sqrt{s} < 11A$ GeV) is very promising for such a measurement since the effect is expected to be sensitive to the baryon density, while the latter happens to reach the maximum in central Au+Au collisions at NICA [16]. Ref. [17] proposed to study the dilepton spectra not only below the ω pole, where the enhancement is observed, but also in the region between the ω and ϕ peaks. As mentioned in [17], in the invariant-mass range of $0.8 < M_{e^+e^-} < 1 \text{ GeV}/c^2$ the in-medium broadening scenario predicts a much higher (up to a factor of 3) dilepton yield than the dropping mass scenario does, and in order to choose the appropriate one the experimental mass resolution of about $10 \text{ MeV}/c^2$ is required.

The experimental study of dileptons in heavy-ion collisions is a challenging task. The main difficulty is a huge combinatorial background of uncorrelated lepton pairs which mainly come from π^0 Dalitz decays and photon conversion in the detector material. Special attention should be paid to reducing this background as much as possible.

The main goal of our study was to develop Monte Carlo algorithms and analysis tools for dielectron reconstruction with the MPD detector and to investigate its performance for low-mass dilepton measurements in terms of the hadron suppression factor, signal-to-background ratio and invariant-mass resolution.

1. DETECTOR SETUP

A detailed description of the MPD detector can be found in [18]. The configuration used in our study includes the Time Projection Chamber (TPC), Time-Of-Flight system (TOF) and

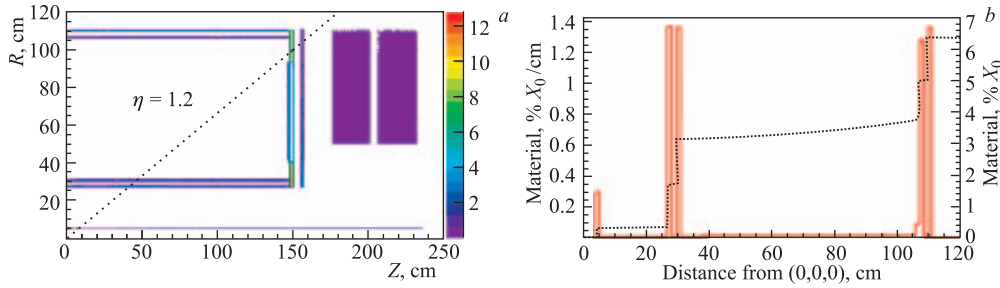


Fig. 1. *a*) Detector material budget in percent of radiation length X_0 . Z and R are the longitudinal and radial coordinates, measured from the detector center (point $(0,0,0)$); the dotted line corresponds to pseudorapidity $\eta = 1.2$ (detector acceptance limit considered). *b*) The detector material vs distance from the detector center at $\eta = 0$. The solid histogram and left scale correspond to the differential distribution, i.e., $\partial(\text{material})/\partial(\text{distance})$, the dotted histogram and right scale are for cumulative distribution, i.e., total material seen from the center. The spikes in the differential distribution correspond to the beam pipe ($R = 5$ cm), inner and outer TPC walls ($R \simeq 30$ and 110 cm)

ElectroMagnetic Calorimeter (EMC) covering the pseudorapidity range $|\eta| < 1.2$. Another relevant detector element is the beam pipe made of beryllium with a wall thickness of 1 mm. The detector material distribution relevant for the current analysis is presented in Fig. 1. One can see that the amount of the material does not exceed 10% of the radiation length in the region of interest.

2. DETECTOR PERFORMANCE

2.1. Track Reconstruction. Since at the current level of detector response simulation the event multiplicity effects do not significantly influence the reconstruction performance, the basic parameters of the MPD setup were studied using large samples of single-particle events of different species (electrons, pions, etc.) with a flat phase-space distribution. Particles were transported through the MPD setup by the Geant 3.21 code and produced hits in the detectors.

The event reconstruction procedures are described in detail in [18] and include track reconstruction in the TPC and track matching with the TOF. The track reconstruction is based on the Kalman filtering technique (see, e.g., [19]). The number of TPC hits per track was required to be greater than 20 to ensure a good precision of the momentum and dE/dx measurements. The efficiency of the track reconstruction, defined as the ratio of the found tracks to the generated ones, is shown in Fig. 2, *a* as a function of the track transverse momentum. All the tracks reconstructed in the TPC were then extrapolated to the TOF detector and matched with TOF hits. The efficiency of track matching with TOF, defined as the ratio between the number of tracks reconstructed in the TPC which have produced a detectable signal in the TOF and the total number of tracks reconstructed in the TPC, was found to be about 90% at $p_T > 0.4$ GeV/ c (see Fig. 2, *a*). The losses are due to dead spaces in the TOF array, interaction with the detector material and inefficiencies of the matching

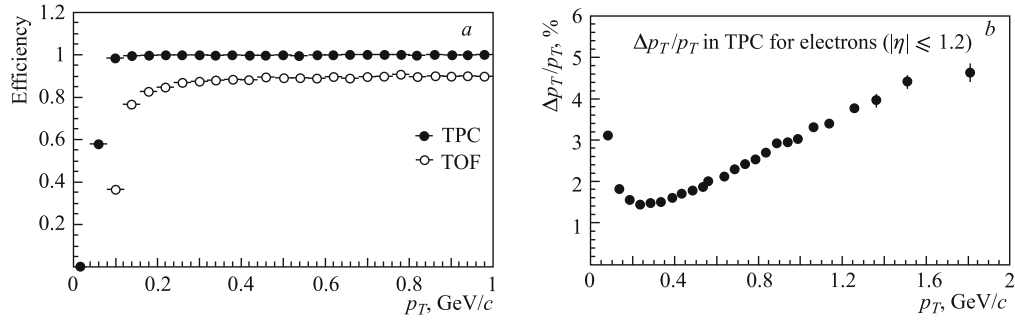


Fig. 2. *a*) The track reconstruction efficiency and TOF matching efficiency as a function of p_T for electrons. *b*) The relative transverse momentum resolution averaged over $|\eta| < 1.2$ for tracks of electrons as a function of p_T

algorithm. The transverse momentum resolution was found to be better than 3% for the tracks with p_T below 1 GeV/c (Fig. 2, *b*).

2.2. Particle Identification (PID). Electron identification is achieved by using combined information about the specific energy loss dE/dx (TPC), time-of-flight (TOF, EMC) and E/p (EMC) measurements. For all the TPC tracks which have a match in the TOF or/and EMC, the electron candidates have been selected by an ellipse cut in the $dE/dx - \beta$ space (Fig. 3). In addition, for the tracks registered by the EMC, the signal from the calorimeter for a given momentum provides another particle identification criterion (Figs. 4 and 5). For tracks without a match in TOF or EMC, a dE/dx -cut is applied for electron selection in some momentum intervals (Fig. 6). The resulting electron selection efficiency, i.e., a fraction of the truly identified electrons, is shown in Fig. 7 as a function of the total momentum. The achieved overall hadron rejection factor is ~ 3200 (Fig. 7). This factor is defined as the ratio of the number of tracks from simulated hadrons, which passed the electron selection criteria, to the number of reconstructed tracks from hadrons.

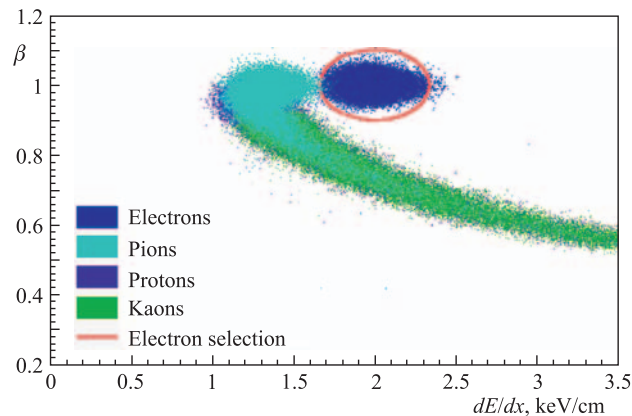


Fig. 3. Reconstructed track velocity versus dE/dx for different particles. The candidates within the ellipse are selected as electrons

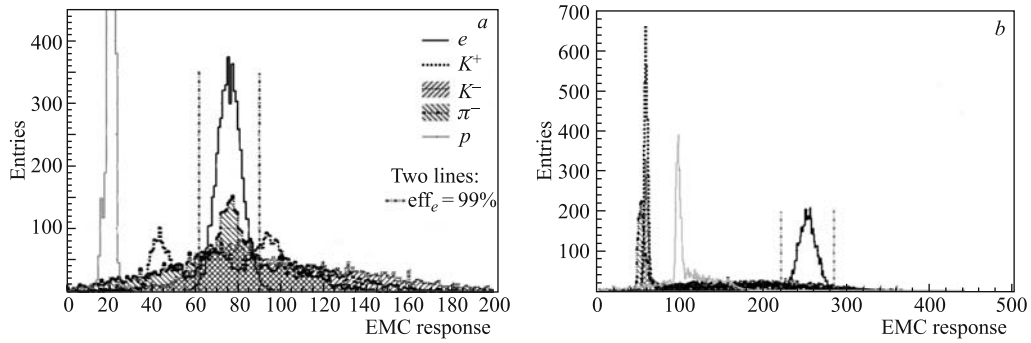


Fig. 4. *a)* EMC response for different particles with a momentum of 0.3 GeV/*c*. *b)* EMC response for the 1.0 GeV/*c* momentum particles. The vertical lines bound the range with the 99% electron selection efficiency

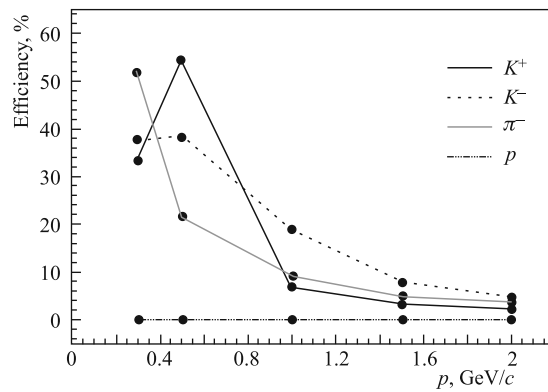


Fig. 5. EMC hadron misidentification efficiency (probability to identify a hadron as an electron), corresponding to 99% electron efficiency, versus the total momentum for different particles

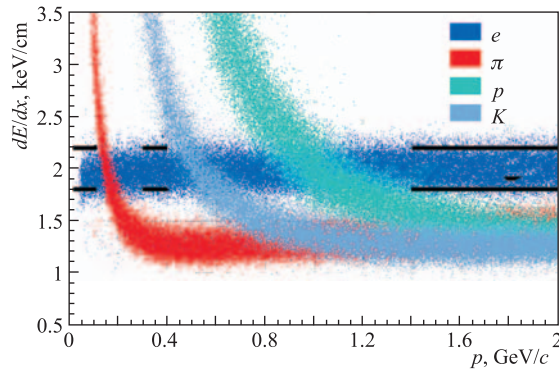


Fig. 6. Reconstructed dE/dx versus momentum for different particles. The thick black lines show the electron acceptance bands and momentum intervals for only dE/dx -based electron selection (for tracks without a match in TOF or EMC)

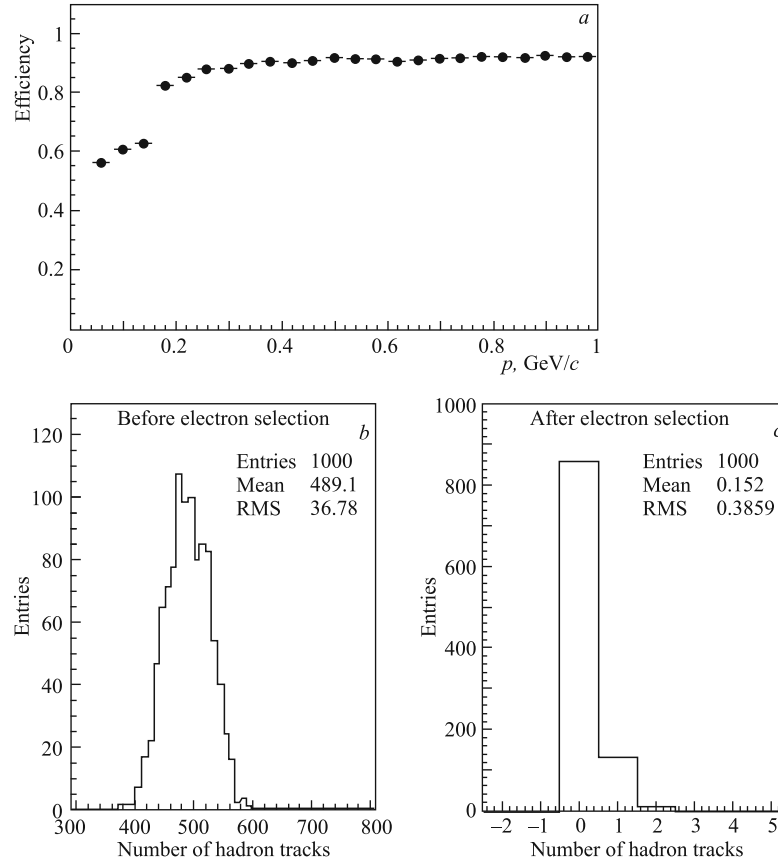


Fig. 7. *a)* The electron selection efficiency versus the total momentum. *b)* The number of the reconstructed tracks from hadrons. *c)* The number of tracks from hadrons that passed the electron selection criteria. The overall (momentum integrated) hadron rejection factor is ~ 3200

3. EVENT GENERATORS

The study of dielectron production in central (0–3 fm) gold–gold collisions at $\sqrt{s} = 7A$ GeV was performed using the Pluto code [20] generating a cocktail of hadrons decaying into the electron–positron or Dalitz electron–positron pairs. The multiplicities of electron sources were predicted by the statistical thermal model [21], the estimated discrepancy between model predictions and experimental data does not exceed a factor of 2 (Fig. 8). The background was calculated by the UrQMD generator [22] which produced hadrons and photons. The events samples have been transported through the detector using the Geant 3.21 transport package (containing photon conversions, etc.). In the UrQMD sample, the tracks from Dalitz decays of π^0 and η were excluded to avoid double counting with Pluto (the heavier mesons from the Pluto cocktail were forced to decay hadronically inside the UrQMD generator). Then, Pluto and UrQMD outputs were mixed as explained below.

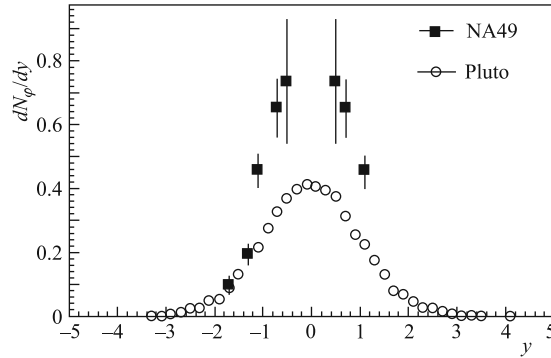


Fig. 8. Rapidity distribution of ϕ mesons from the Pluto generator as compared to the data from the NA49 experiment [26]. Note that the experimental points correspond to the collisions of heavier nuclei (Pb + Pb) at higher energies ($\sqrt{s} = 7.6A$ GeV)

4. ANALYSIS PROCEDURE

4.1. Track Selection. To ensure the track quality, the following criteria were applied: $|\eta| < 1.2$, number of track space points in the TPC larger than 20 and the track should come from the primary vertex; i.e., the distances of the closest approach to the primary vertex in the transverse and longitudinal directions are within 3σ of the respective distributions for primary tracks.

4.2. Event Samples. Since the full analysis chain includes transport of particles through the detector, track reconstruction and particle identification procedures, and is therefore quite time consuming, we have used a simplified approach when only a relatively small number of central gold–gold collisions (10^4) from the UrQMD generator (which determines the background) was simulated and then mixed with $2 \cdot 10^7$ events from Pluto (the latter corresponds to ~ 18 h of running time at the NICA collision rate of 6 kHz). The event mixing procedure was realized as follows: the UrQMD event sample was fully processed and all the tracks that passed the electron identification criteria plus extra acceptance cuts (see below) were stored as a common track pool. Then, for each Pluto event, a random track selection from this pool was done with the requirement to reproduce the residual UrQMD track multiplicity distribution (Fig. 11).

4.3. Background Suppression. Since the particle identification suppresses the hadron contamination, the main source of the remaining background is photon conversion in the detector material. The conversion pairs can be rejected by a topological cut, making use of the fact that the electron–positron pair is produced with almost zero opening angle. In the magnetic field the particle trajectories are deflected in such a way that the plane formed by the electron and positron momenta is oriented mainly perpendicular to the magnetic field direction (the normal to the plane is mostly parallel to the magnetic field) [12]. We have complemented this value by the radial position of the production point of the dielectron and applied a 2-dimensional cut (Fig. 9). This cut removes the majority of the conversion pairs. However, if only one lepton from a conversion pair is reconstructed, it can survive the cut. To suppress such tracks further, we have applied a low-momentum cut: $p_T > 200$ MeV/c (Fig. 10). A high-momentum cut ($p < 2$ GeV/c) was also applied to decrease the residual hadron (mostly proton) contamination. The final background multiplicity distribution from

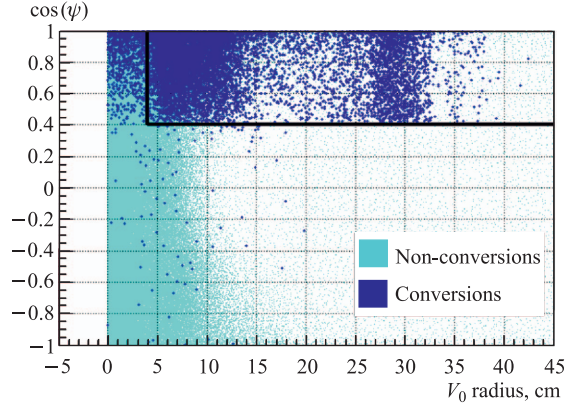


Fig. 9. Cosine of the angle between the normal to the plane, defined by the electron–positron pair, and the magnetic field direction (ψ) versus the reconstructed radial position of the pair origin (V_0): blue symbols (small crosses) represent conversion pairs, the cyan ones (dots) — the others. The rectangular region represents the conversion rejection cut

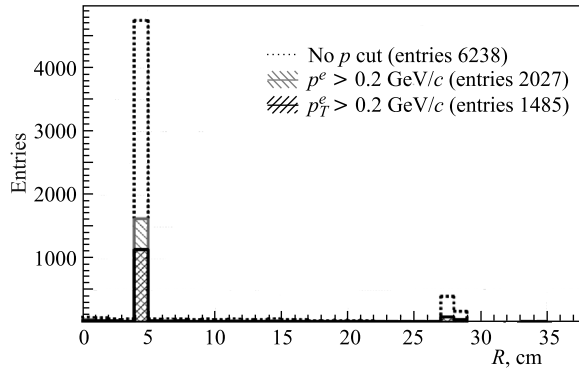


Fig. 10. True radial positions of points of the photon conversion, giving either a reconstructed electron or positron (or both) after applying the topological cut (Fig. 9), for 10 000 UrQMD events. A low- p^e or low- p_T^e cut helps to reject conversion tracks

UrQMD is shown in Fig. 11 in comparison with the signal one from Pluto. One can see that the residual hadron contamination is $\sim 1.5\%$.

In order to improve the signal-to-background ratio, we have applied the so-called « π^0 »-rejection procedure as described in [8]. The essence of this procedure consists in the following: for each electron–positron combination with the invariant mass below $0.2 \text{ GeV}/c^2$, both tracks are excluded from further pairing because of being the products of the Dalitz decay of π^0 . Ref. [23] offered an additional selection criterion based on the geometrical mean value of the pair momenta $\sqrt{|\mathbf{p}_{e^+}||\mathbf{p}_{e^-}|}$. Since this value has different distributions for electron–positron pairs from the decays of vector mesons and those for random combinations (Fig. 12), the cut $\sqrt{|\mathbf{p}_{e^+}||\mathbf{p}_{e^-}|} > 0.3 \text{ GeV}/c$ turned out to be useful.

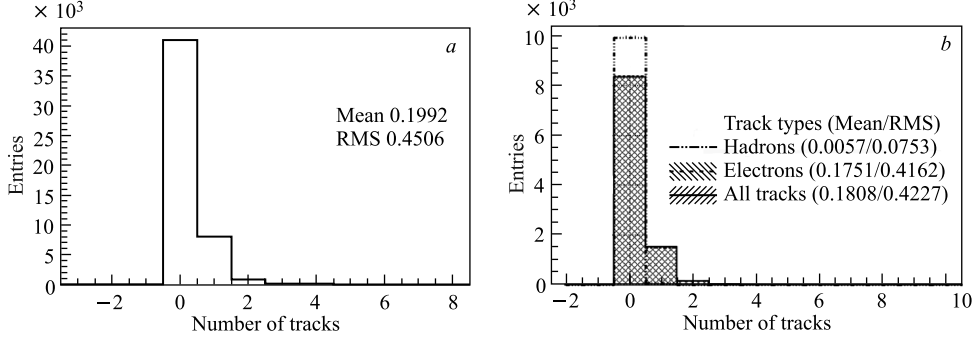


Fig. 11. Track multiplicity distributions after the final selection: *a*) signal (electrons/positrons from Pluto); *b*) background (electrons/positrons, hadrons and all tracks from UrQMD)

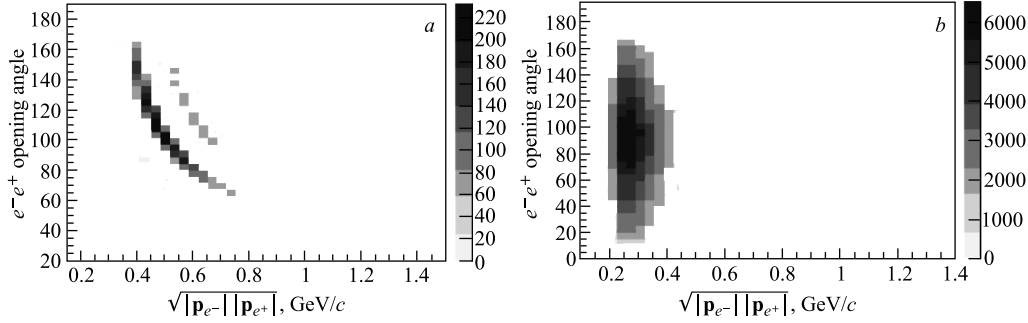


Fig. 12. *a*) Electron–positron opening angle as a function of their momentum geometrical mean value $\sqrt{|\mathbf{p}_{e^+}||\mathbf{p}_{e^-}|}$ for vector mesons ρ , ω , ϕ . *b*) The same plot for background pair combinations. The cut $\sqrt{|\mathbf{p}_{e^+}||\mathbf{p}_{e^-}|} > 0.3$ GeV/ c removes a large fraction of background combinations

5. RESULTS AND DISCUSSION

Figure 13 shows the invariant-mass distributions of electron–positron pairs (panels *a*, *b*) and signal-to-background ratios in bins of the invariant mass (*c*, *d*) for two pseudorapidity windows: $|\eta| < 0.5$ and $|\eta| < 1.0$. The signal-to-background ratio (S/B) is defined as the ratio of the number of e^+e^- combinations from meson decays to that of all the other electron–positron combinations. There is an apparent advantage, in terms of the signal-to-background (S/B) ratio, of using a smaller detector pseudorapidity acceptance due to stronger dependence of the statistics of the combinatorial background on the acceptance width (signal statistics depends linearly on multiplicity, while the background scales quadratically with it). However, the acceptance restriction causes a loss of signal, which can be partially reduced if a slightly different constraint is used; i.e., a pair is formed only if two tracks lie within some interval of pseudorapidity $\Delta\eta$ (table). Moreover, it is expected that a larger diameter of the beam pipe provides better conditions for rejecting unpaired conversion electrons produced inside the pipe wall due to their larger overall distance of the closest approach to the primary vertex («primary vertex origin»-cut). In the last column of the table there are results for

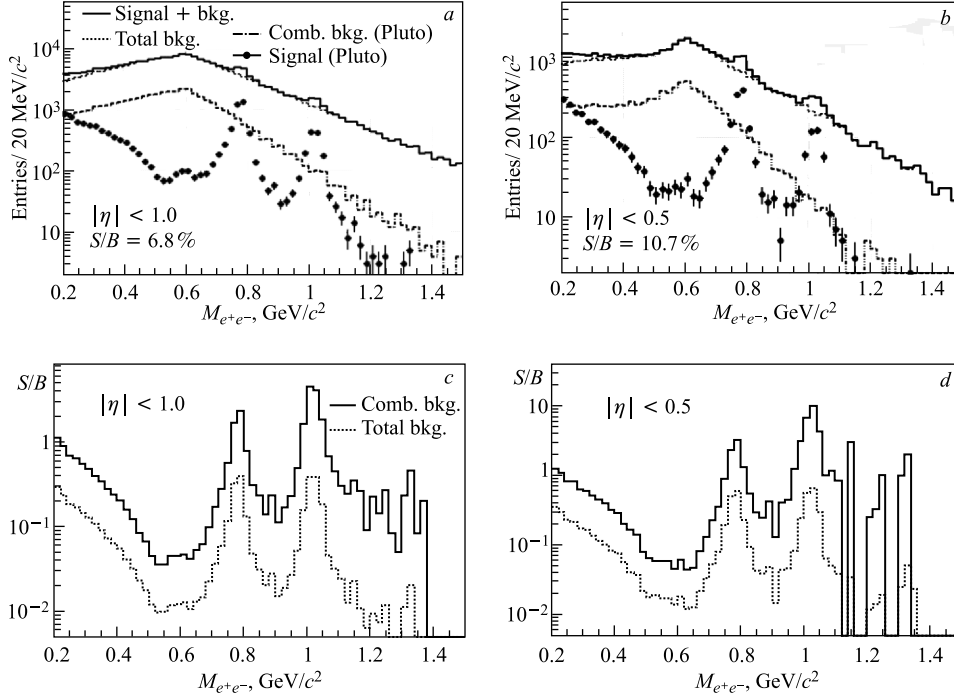


Fig. 13. *a, b*) Reconstructed invariant mass of electron–positron pairs; *c, d*) signal-to-background ratios in invariant-mass bins. Also shown are the integrated signal-to-background ratios for invariant-mass values of 0.2–1.5 GeV/c^2

a beam pipe of the diameter four times larger than the nominal one and, indeed, we have observed increase of the S/B ratio.

The obtained results for the signal-to-background ratio are shown in Fig. 14 along with the published data from other experiments.

A rough estimate of the invariant-mass resolution of the MPD setup was made by fitting the dilepton spectra at ω and ϕ poles: RMS of 14 and 17 MeV/c^2 was obtained for ω and ϕ , respectively.

Number of selected signal e^+e^- pairs and signal-to-background ratio, defined as the ratio of numbers of signal and background e^+e^- combinations with the invariant mass from 0.2 to 1.5 GeV/c^2 , for different detector pseudorapidity acceptance $|\eta|$ and different cuts on e^+e^- pseudorapidity distance $|\Delta\eta_{e^+e^-}|$. Signal-to-background ratios are shown for setups with the beam pipe radius of 5 and 20 cm

Detector acceptance $ \eta $	$ \Delta\eta_{e^+e^-} $	Signal	$S/B, \%$	
			$R_{\text{pipe}} = 5 \text{ cm}$	$R_{\text{pipe}} = 20 \text{ cm}$
< 1.0	—	13025	6.8	10.7
< 0.5	—	3754	10.1	12.7
< 1.2	< 1.0	14198	8.2	13.2
< 1.2	< 0.5	8616	9.4	15.7
< 1.2	< 0.25	4531	9.6	16.8

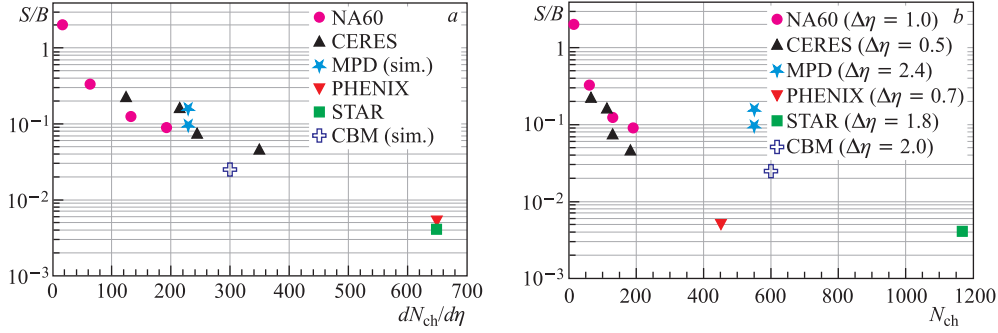


Fig. 14. Signal-to-background ratios obtained in different experiments: *a*) versus charged particle density; *b*) versus the number of charged particles in the detector acceptance. The numbers are for the CERES [7–10], NA60 [11], PHENIX [12], STAR [13], CBM [27] and MPD setups (4th columns from the table). The MPD results are shown for the two beam pipe settings (see the text)

6. SUMMARY AND PLANS

Simulation of electron measurements in the MPD detector at NICA was performed for central Au + Au collisions at $\sqrt{s} = 7A$ GeV. Performance of the MPD setup for electron tracking and identification as well as for reconstruction of the dilepton invariant-mass spectra was studied. The achieved hadron suppression factor (below 10^{-4}) allowed us to get a signal-to-background ratio of about 0.1 for $0.2 < M_{e^+e^-} < 1.5$ GeV/ c^2 . The achieved significance is comparable or better than those in the existing experimental setups.

Since it is planned to have an extended MPD geometry available for dielectron studies (up to $|\eta| < 2.0$), it will be necessary to evaluate the impact of the extended configuration on the dielectron physics; i.e., the full analysis chain should be exercised for the extended setup, including track reconstruction and particle identification in the endcap region.

The installation of the inner tracking system made of silicon detectors would also affect the detector performance due to additional amount of material and, on the other hand, better determination of track parameters near the interaction region.

The experimentally observed enhancement of the dielectron spectra in the invariant-mass region of 0.2–0.6 GeV/ c^2 needs new mechanisms of vector meson formation in a dense nuclear matter for its explanation, e.g., as proposed and implemented in the event generators QGSM [24] and HSD [25], which are planned to be used for better estimations of the signal-to-background ratio.

Acknowledgements. We would like to thank Prof. I. Tserruya for many useful discussions. The authors are grateful to S. V. Chubakova for help in the preparation of the paper.

REFERENCES

1. Sissakian A. N., Sorin A. S. // J. Phys. G: Nucl. Part. Phys. 2009. V. 36. P. 064069.
2. Alt C. et al. (NA49 Collab.) // Rhys. Rev. C. 2008. V. 78. P. 024903.
3. Rapp R., Wambach J. // Adv. Nucl. Phys. 2000. V. 25. P. 1.
4. Hatsuda T., Lee S. H. // Phys. Rev. C. 1992. V. 46. P. R34.

5. Rapp R., Chanfray G., Wambach J. // Phys. Rev. Lett. 1996. V. 76. P. 368.
6. Brown G. E., Rho M. // Phys. Rev. Lett. 1991. V. 66. P. 2720.
7. Agakichiev G. et al. (CERES Collab.) // Phys. Lett. B. 1998. V. 422. P. 405.
8. Adamova D. et al. (CERES Collab.) // Phys. Rev. Lett. 2003. V. 91. P. 042301.
9. Agakichiev G. et al. (CERES Collab.) // Eur. Phys. J. C. 2005. V. 41. P. 475.
10. Adamova D. et al. (CERES Collab.) // Phys. Lett. 2008. V. 666. P. 425.
11. Arnaldi R. et al. (NA60 Collab.) // Phys. Rev. Lett. 2006. V. 96. P. 162302.
12. Adare A. et al. (PHENIX Collab.) // Phys. Rev. C. 2010. V. 81. P. 034911.
13. Xin Dong (STAR Collab.). arXiv:1210.6677v1[nucl-ex].
14. Porter R. J. et al. (DLS Collab.) // Phys. Rev. Lett. 1997. V. 79. P. 1229.
15. Rustamov A. et al. (HADES Collab.) // Intern. J. Mod. Phys. A. 2011. V. 26. P. 384.
16. Randrup J., Cleymans J. // Phys. Rev. C. 2006. V. 74. P. 047901.
17. Cassing W. et al. // Phys. Rev. C. 1998. V. 57. P. 916.
18. http://nica.jinr.ru/files/CDR_MPD/MPD_CDR_en.pdf
19. Fruehwirth R. // Nucl. Instr. Meth. A. 1987. V. 262. P. 444.
20. Froehlich I. et al. arXiv:0708.2382v2[nucl-ex].
21. Braun-Munzinger P., Redlich K., Stachel J. Invited Review for Quark Gluon Plasma 3. World Sci. Publ., 2004. P. 491; arXiv:nucl-th/0304013.
22. <http://urqmd.org/>
23. Galatyuk T. PhD Thesis. J. W. Goethe Universität. Frankfurt am Main, 2009.
24. Bravina L. V. et al. // Nucl. Phys. A. 1994. V. 566. P. 461c.
25. Cassing W., Bratkovskaya E. L., Juchem S. // Nucl. Phys. A. 2000. V. 674. P. 249.
26. Alt C. et al. (NA49 Collab.) // Phys. Rev. C. 2008. V. 78. P. 044907.
27. Galatyuk T. Exploring Phase Diagram of Matter with Virtual Photons // <http://www-aix.gsi.de/conferences/emmi/epd2012/>.

Received on January 30, 2013.